Direct Power Distribution Strategy Based on Space Vector Modulation for Single-Stage Dual-DC-Port Inverter

Lijie Liu, *Member, IEEE*, Dehong Zhou, *Senior Member, IEEE*, Jianxiao Zou, *Member, IEEE*, and Zewei Shen, *Member, IEEE*

***Abstract*—The single-stage dual-dc-port inverter directly connects the photovoltaic-battery hybrid system to the ac side, which offers the advantages of high efficiency and low cost due to the removal of dc–dc converter. The existing modulation-based power distribution strategies realize flexible power flow control by indirectly regulating redundant zero or small vectors via additional outer loop power controllers, which have the drawbacks of limited steady-state and dynamic response. To address this issue, the relationship between the dc-port power and large/small vectors is analytically revealed, which provides intuitive parameter design guidelines for power distribution control. On this basis, a direct power distribution strategy based on space-vector modulation is proposed, which regulates the dc-port power by splitting the reference voltage vector into large and small vectors. Compared to the conventional strategies, the proposed strategy shows better steady-state and dynamic response due to desirable power control directly realized in the modulation layer. Finally, the comprehensive comparison experimental tests are conducted to verify the effectiveness and advantages of the proposed direct power distribution strategy.**

***Index Terms*—Photovoltaic (PV)-battery hybrid system, power distribution, single-stage dual-dc-port inverter (SDI), space-vector modulation (SVM).**

Nomenclature

PV	Photovoltaic.
ESS	Energy storage system.
SDI	Single-stage dual-dc-port inverter.
NPC	Neutral-point-clamped.
SoC	State of charge.
PWM	Pulsewidth modulation.
SVM	Space-vector modulation.
PI	Proportional-integer.
A/D	Analog to digital.
RMS	Root mean square.
THD	Total harmonic distortion.

Received 9 October 2024; revised 9 January 2025 and 24 February 2025; accepted 25 March 2025. Date of publication 28 March 2025; date of current version 26 May 2025. This work was supported in part by the National Natural Science Foundation of China under Grant 62173067, in part by the Guangdong Basic and Applied Basic Research Foundation under Grant 2024A1515010184 and Grant 2023A1515240060, in part by the Guangdong Science and Technology Program under Grant 2021QN02L854, in part by the Sichuan Science and Technology Program under Grant 2023NSFSC0298, and in part by the Shenzhen Science and Technology Program under Grant JCYJ20220530165001003, Grant JCYJ20230807120006012, and Grant JSGG20220831110805010. Recommended for publication by Associate Editor D. O. Neacsu. *(Corresponding author: Dehong Zhou.)*

Lijie Liu is with the School of Electrical Engineering, Chongqing University, Chongqing 400044, China (e-mail: liulijie@cqu.edu.cn).

Dehong Zhou, Jianxiao Zou, and Zewei Shen are with the School of Automation Engineering, University of Electronic Science and Technology of China, Chengdu 611731, China, and also with the Shenzhen Institute for Advanced Study, University of Electronic Science and Technology of China, Shenzhen 518110, China (e-mail: dhzhou@uestc.edu.cn; jxzou@uestc.edu.cn; shenzw@uestc.edu.cn).

Color versions of one or more figures in this article are available at https://doi.org/10.1109/TPEL.2025.3555664.

Digital Object Identifier 10.1109/TPEL.2025.3555664

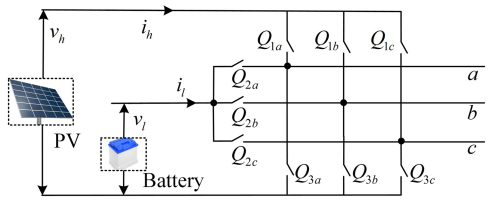

Fig. 1. Configuration of SDI-connected PV-battery hybrid system.

I. Introduction

PV GENERATION technologies offer attractive solutions for alleviating environmental pollution and energy shortage problems [1], [2]. PV generation technologies have drawn considerable attention due to their advantages of being clean, sustainable, and low-cost. However, they also have the disadvantage of intermittent due to unpredictable natural conditions, for instance, the weather. To solve this problem, energy storage systems are usually adopted to smooth power fluctuations in PV generation systems [3], [4]. As a result, numerous advanced strategies have been investigated for PV-battery hybrid systems in recent years [5], [6].

The SDI provides an attractive solution for integrating the PV-battery hybrid system. Two dc ports of SDI are directly connected to the PV-battery hybrid system, as shown in Fig. 1. Due to the salient advantages of high integration, this architecture has been widely used in multisource applications, for instance, hybrid electric vehicles [7], [8], [9], [10]. The SDI-based solution improves system efficiency at the topology level. The system efficiency can also be improved from the device level [11], [12], such as wide bandgap devices. Compared to the conventional two-stage topologies, the SDI can improve efficiency

TABLE I
COMPARISON OF THE EXISTING SVM-BASED POWER DISTRIBUTION STRATEGIES

REF	Basic idea	Computational burden	Steady state accuracy	Dynamic response
[31], [32]	Select small vectors via PI controller	High	Low	Slow
[33]	Regulate small vectors via PI controller	High	Low	Slow
[34]	Regulate zero vectors via PI controller	Medium	Low	Slow
[35]	Regulate dc-port power via PI controller	Medium	Low	Slow
Proposed method	Direct distribute power via SVM	Medium	High	Fast

and reduce cost due to: 1) DC–dc converter and its filter are removed; 2) single-stage power flow can be obtained [13], [14], [15]. By replacing the ideal switches with switching devices in Fig. 1, two different SDI topologies can be achieved, namely NPC form [16], [17] and T-type neutral-point-clamped (T-NPC) form [18], [19] SDIs.

The circuit structure of SDI is similar to that of conventional multilevel converters. Although various modulation strategies have been proposed for multilevel converters [20], [21], [22], [23], [24], [25], they could not be transplanted to SDI. First of all, the dc-port voltages of SDI are usually unbalanced due to the voltages of the PV-battery hybrid system being variable with natural conditions (weather, temperature) and state of charge (SoC). Conventional PWM strategies [20], [21], [22], [23], [24], [25] are only suitable for balanced dc-port voltages, which is ineffective in the case of unbalanced dc-port voltages. Moreover, the modulation target of SDI is to realize flexible power distribution between the PV unit and battery, rather than keep the dc-port voltage balance in conventional modulation strategies [20], [21], [22], [23], [24], [25]. In summary, the PWM strategy for SDI should offer desirable dc-port power distribution capability with the unevenly distributed space vector diagram.

Regarding the modulation design for the unevenly distributed space vector diagram, some previous studies provide effective solutions. A virtual SVM was proposed for the unbalanced dc-link voltages, which can adjust the unbalancing degree with high accuracy for any modulation indexes and load power factors [26]. An improved SVM is investigated to reduce the common-mode voltage in the case of unbalanced dc-port voltages [27]. An analytical discontinuous SVM was proposed to suppress output harmonics and maximize the linear modulation region under unbalanced dc-link voltages [28]. A modified SVM was proposed for improving system efficiency [29]. The symmetrical SVM was proposed for realizing low current harmonics in the case of unbalanced and oscillated dc-link voltages [30]. Although the abovementioned modulation strategies are effective for the unevenly distributed vector space diagram and have achieved desirable performance, they cannot be directly applied for SDI due to the lack of power distribution ability.

Regarding the power distribution issue of the SDI, substantial SVM-based methods have been studied recently. To realize power delivery between two dc ports, the modified SVM is proposed in [31] and [32]. The basic idea is to select different small vectors in the process of reference voltage vector synthesis. A virtual SVM is proposed for flexible power control by regulating the redundant small vectors [33]. However, complicated calculations are unavoidable due to the uneven voltage vectors being directly used [31], [32], [33]. Desirable power distribution control is realized by controlling the redundant zero vectors in the modified SVM strategy [34]. A decoupled model-based modulation is proposed for dc-port power distribution in [35]. Unfortunately, these strategies share a common issue in that the power distribution is realized by indirectly regulating redundant vector components via the additional PI controllers. As a result, the steady-state/dynamic performance of power distribution control is limited. Table I shows the comparison of the existing SVM-based power distribution strategies. Therefore, an intuitive but effective power distribution strategy is urgently required for SDI.

To deal with the aforementioned issues, a direct power distribution strategy based on SVM is proposed for SDI. First, the analytical relationship between dc-port power and space vector is established, which offers detailed parameter design guidelines for power distribution. Then, flexible power distribution is realized by splitting the reference voltage vector into large and small vectors. Complicated calculations caused by the uneven space vectors can be avoided by synthesizing the split vectors via two-level modulation. Due to flexible power distribution being directly realized in the modulation layer, better steady state, and dynamic performance can be achieved compared to conventional SVM-based strategies. Finally, experimental tests have been carried out to verify the effectiveness of the proposed direct power distribution strategy.

The rest of this article is organized as follows. The SDI-connected PV-battery hybrid system is illustrated in Section II. Section III provides the proposed direct power distribution strategy based on SVM. The experimental results are shown in Section IV to verify the effectiveness of the proposed solution. Finally, Section V concludes this article.

II. SDI-CONNECTED PV-BATTERY HYBRID SYSTEM

In this section, the topology of an SDI-connected PV-battery hybrid system is given first. Then, the space vector diagram of SDI is introduced.

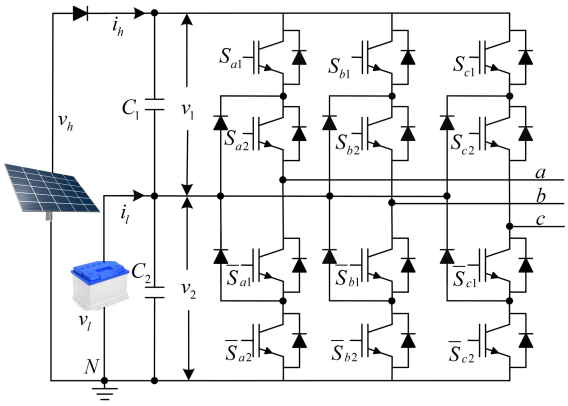

Fig. 2. Topology of SDI-connected PV-battery hybrid system.

TABLE II
SWITCHING STATES AND OUTPUT VOLTAGES

$S_{x1}S_{x2}\overline{S}_{x1}\overline{S}_{x2}$	S_x	Output voltage
1100	2	v_1+v_2
0110	1	v_2
0011	0	0

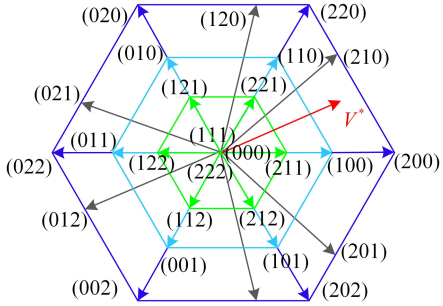

Fig. 3. Space vector diagram under DC-port voltage ratio $\gamma < \frac{1}{2}$.

A. Topology of SDI-Connected PV-Battery Hybrid System

Fig. 2 shows the topology of an SDI-connected PV-battery hybrid system. The SDI can be considered a modified three-level NPC converter with unequal dc port voltages, which directly connects the PV-battery hybrid system to ac side. The dc port with lower voltage v_l is connected to the battery, and the dc port with higher voltage v_h is connected to the PV unit. The voltages of the dc-side capacitor are $v_1 = v_h - v_l$ and $v_2 = v_l$. The output currents of the PV unit and battery are i_h and i_l, respectively. Switching states and output voltages of the SDI in phase $x(x = a, b, c)$ are given in Table II. It is well-known that the voltages of PV-battery hybrid system are determined by the natural conditions and SoC. As a result, the dc-link voltages are usually unbalanced, making the space vector diagram unevenly distributed.

B. Space Vector Diagram of SDI

Fig. 3 gives the space vector diagram under dc-port voltage ratio $\gamma < \frac{1}{2}$. The dc-port voltage ratio is defined as $\gamma = \frac{v_1}{v_1+v_2}$.

TABLE III
CLASSIFICATION OF VOLTAGE VECTORS IN SDI

Voltage vectors	Switching states
Zero vectors $\boldsymbol{V_Z}$	(222),(111),(000)
Positive small vectors $\boldsymbol{V_{Py}}$	(100),(110),(010),(011),(001),(101)
Negative small vectors $\boldsymbol{V_{Ny}}$	(211),(221),(121),(122),(112),(212)
Medium vectors $\boldsymbol{V_{My}}$	(210),(120),(021),(012),(102),(201)
Large vectors $\boldsymbol{V_{Ly}}$	(200),(220),(020),(022),(002),(202)

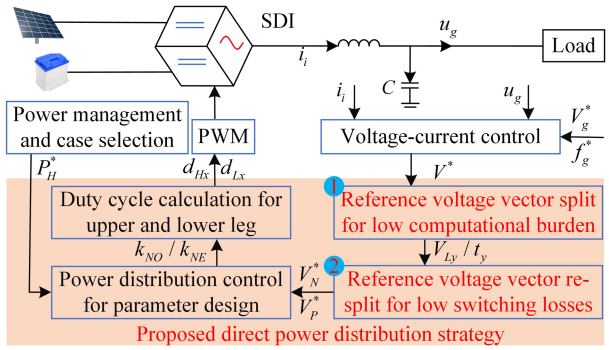

Fig. 4. Overall block diagram for the proposed direct power distribution strategy based on SVM.

The space vector diagrams under $\gamma = \frac{1}{2}$ and $\gamma > \frac{1}{2}$ are not given because they are similar to Fig. 3. Table III shows the classification of voltage vectors. The total voltage vectors are classified into five categories, i.e., zero vectors $\boldsymbol{V_Z}$, positive small vectors $\boldsymbol{V_{Py}}$, negative small vectors $\boldsymbol{V_{Ny}}$, medium vectors $\boldsymbol{V_{My}}$, and large vectors $\boldsymbol{V_{Ly}}$. As shown in Fig. 3, the voltage vectors are unevenly distributed due to the unbalanced dc-link voltages. It is challenging to design the modulation strategy to generate the reference voltage vector $\boldsymbol{V}^*$ in the asymmetrical three-level converter frame. In addition, flexible power distribution between the PV unit and the battery should be realized by modulation. A direct power distribution strategy based on SVM is proposed, which will be detailed in Section III.

III. Proposed Direct Power Distribution Strategy Based on SVM

The overall block diagram for the proposed direct power distribution strategy based on SVM is illustrated in Fig. 4. The system operates in islanded microgrid mode, and the SDI connects the ac load via the LC filter. The grid-forming control structure is presented for SDI, and the well-known voltage-current double-loop PI control is used to track the reference of amplitude V_g^* and frequency f_g^* of grid voltage. The external loop controls the grid voltage u_g to match its reference, while the internal control loop regulates the inverter-side current i_i. The detailed control block of the voltage-current double-loop PI control can be found in [36]. On the dc side, the power management strategy is adopted to generate the reference output power of PV unit P_H^*. According to the PV MPPT and SoC of the battery, three different operation cases are considered in this study [37], [38]. In case 1, the PV unit and battery support the grid together. In case 2, only the PV unit supports the grid. In case

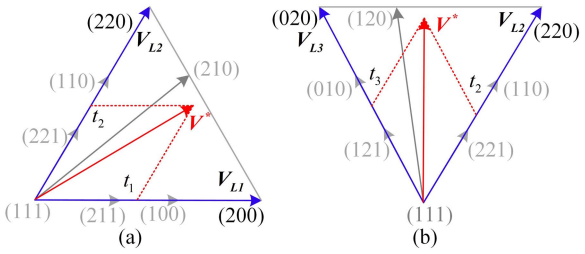

Fig. 5. Reference voltage vector split by large vectors. (a) In Sector I. (b) In Sector II.

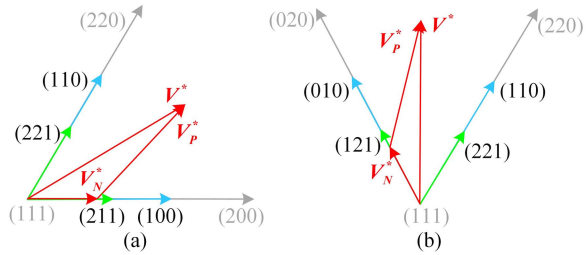

Fig. 6. Reference voltage vector resplit with small vectors. (a) In Sector I. (b) In Sector II.

3, the PV unit not only supports the grid but also charges to the battery. Under constant grid power, flexible power distribution between the PV unit and battery can be realized by tracking P_H^*. The contribution of this article is the proposed direct power distribution strategy based on SVM, which is responsible for dc-port power distribution.

In the following text, the details of the proposed direct power distribution strategy will be given, including reference voltage vector split for low computational burden, reference voltage vector resplit for low switching losses, power distribution control for parameter design, and duty cycle calculation for the upper and lower legs.

A. Reference Voltage Vector Split for Low Computational Burden

For the sake of simplicity, only the voltage vectors in Sectors I and II are discussed. To avoid complicated calculations, the reference voltage vector is split into large vectors in the first stage. As shown in Fig. 5, the reference voltage vector $\boldsymbol{V}^*$ can be expressed as follows:

$$\begin{cases} \boldsymbol{V}^* = \frac{\boldsymbol{V_{L1}}t_1+\boldsymbol{V_{L2}}t_2}{T_s}, \text{In Sector I} \\ \boldsymbol{V}^* = \frac{\boldsymbol{V_{L2}}t_2+\boldsymbol{V_{L3}}t_3}{T_s}, \text{In Sector II} \end{cases} \tag{1}$$

where $\boldsymbol{V_{L1}}/\boldsymbol{V_{L2}}/\boldsymbol{V_{L3}}$ is the large vector of SDI in Sector I and II, $t_1/t_2/t_3$ is the virtual dwell time of large vector, and T_s is the sampling period. The sum of the dwell time of the vectors should be less than the switching period, i.e., $t_1 + t_2 < T_s$ and $t_2 + t_3 < T_s$. By doing this, the computational burden caused by the uneven vectors can be avoided.

B. Reference Voltage Vector Resplit for Low Switching Losses

To reduce the switching losses, the reference voltage vector is decomposed into two parts that can be generated by negative and positive small vectors, respectively. As shown in Fig. 6, the reference voltage vector can be rewritten as

$$\boldsymbol{V}^* = \boldsymbol{V_N^*} + \boldsymbol{V_P^*} \tag{2}$$

where $\boldsymbol{V_N^*}/\boldsymbol{V_P^*}$ is the decomposed reference vector. $\boldsymbol{V_N^*}$ can be directly generated by the negative small vectors due to the same direction, for instance, (211) in Sector I. $\boldsymbol{V_P^*}$ can be synthesized by the positive small vectors, for instance, (110)/(100) in Sector I. To minimize the switching times of SDI, the zero vector is selected as (111). The negative small vectors (211) and (121) in Sectors I and II are selected, respectively.

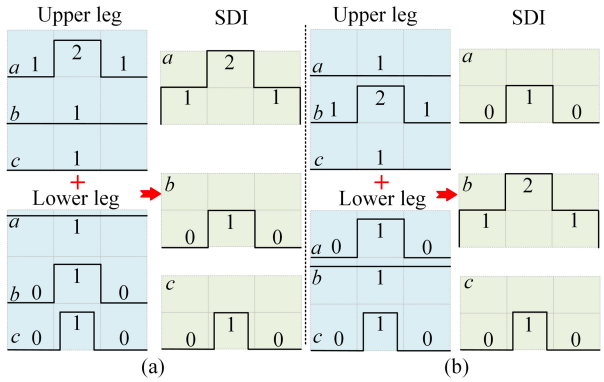

Fig. 7. Switching state of upper leg, lower leg, and SDI. (a) In Sector I. (b) In Sector II.

As shown in Fig. 6(a), the direction of $\boldsymbol{V_N^*}$ is the same as that of the negative small vector (211). Then, $\boldsymbol{V_N^*}/\boldsymbol{V_P^*}$ can be expressed as

$$\begin{cases} \boldsymbol{V_N^*} = \frac{k_{\text{NO}}\boldsymbol{V_{L1}}t_1}{T_s} \\ \boldsymbol{V_P^*} = \frac{(1-k_{\text{NO}})\boldsymbol{V_{L1}}t_1+\boldsymbol{V_{L2}}t_2}{T_s} \end{cases} \tag{3}$$

where k_{NO} is the proportional factor for regulating the odd large vector $\boldsymbol{V_{L1}}/\boldsymbol{V_{L3}}/\boldsymbol{V_{L5}}$, $0 \le k_{\text{NO}} \le 1$. Similarly, the direction of $\boldsymbol{V_N^*}$ is the same as that of the negative small vector (121) in Fig. 6(b). In Sector II, $\boldsymbol{V_N^*}/\boldsymbol{V_P^*}$ can be expressed as

$$\begin{cases} \boldsymbol{V_N^*} = \frac{k_{\text{NO}}\boldsymbol{V_{L3}}t_3}{T_s} \\ \boldsymbol{V_P^*} = \frac{(1-k_{\text{NO}})\boldsymbol{V_{L3}}t_3+\boldsymbol{V_{L2}}t_2}{T_s}. \end{cases} \tag{4}$$

Fig. 7 shows the switching state of the upper leg, lower leg, and SDI: (a) in Sector I, (b) in Sector II. For the upper leg, the switching states of two phases are fixed. There is only one switching action for the upper leg. Hence, decomposing the reference voltage vector into small vectors is an effective solution to reduce switching losses.

C. Power Distribution Control for Parameter Design

1) Basic Idea of Power Distribution: The power paths of small vectors are used to illustrate the basic idea of power distribution. Fig. 8 shows the power paths of small vectors in Sector I: (a) negative small vectors, (b) positive small vectors.

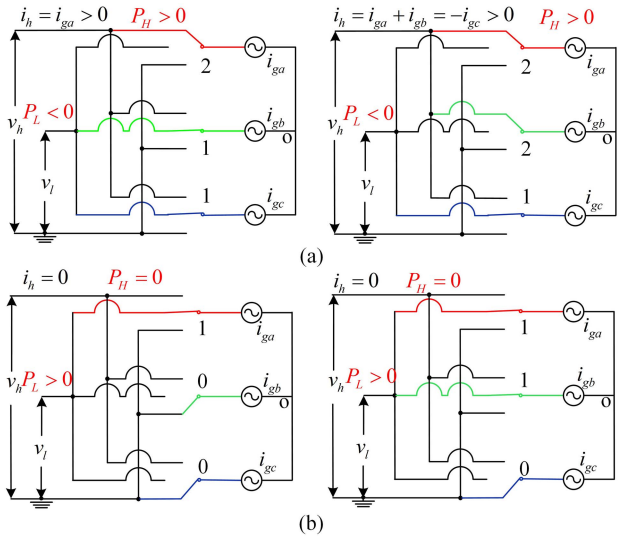

Fig. 8. Power paths of small vectors in Sector I. (a) Negative small vectors. (b) Positive small vectors.

TABLE IV
SELECTED NEGATIVE SMALL VECTORS IN POWER DISTRIBUTION PROCESS

Sector	I	II	III	IV	V	VI
Primary	(211)	(121)	(121)	(112)	(112)	(211)
Secondary	(221)	(221)	(122)	(122)	(212)	(212)

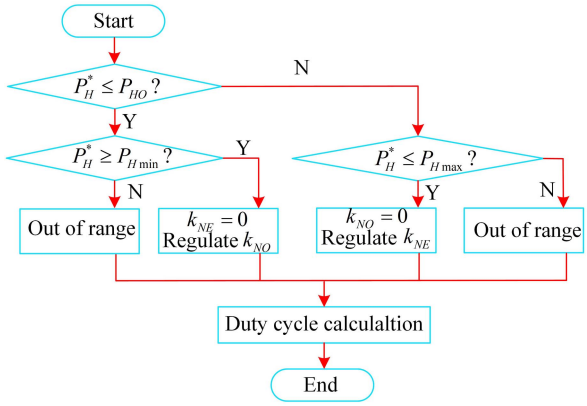

Fig. 9. Flowchart of the proposed power distribution strategy.

In Fig. 8(a), the battery power $P_L < 0$ should be satisfied with negative small vectors. In Fig. 8(b), the battery power $P_L > 0$ should be satisfied with positive small vectors. And the PV port power $P_H > 0$ and $P_H = 0$ can be achieved in Fig. 8(a) and (b), respectively. Hence, the maximum value of PV port power $P_{H\max}$ can be obtained when all negative small vectors are used

$$P_{H\max} = P_{\rm HO} + P_{\rm HE} \tag{5}$$

where $P_{\rm HO}$ indicates the active power provided by the odd negative small vector $\boldsymbol{V_{N1}/V_{N3}/V_{N5}}$, i.e., (211)/(121)/(112)

$$P_{\rm HO} = \frac{3}{2}{\rm Re}(\bar{\boldsymbol{i}}\boldsymbol{V_{Ny}}) = \frac{3}{2\gamma}{\rm Re}\left(\bar{\boldsymbol{i}}\frac{\boldsymbol{V_{Ly}}t_y}{T_s}\right), y = 1, 3, 5 \tag{6}$$

where $\bar{\boldsymbol{i}}$ means the conjugate of grid-side current vector $\boldsymbol{i}$. $P_{\rm HE}$ indicates active power provided by the even negative small vector $\boldsymbol{V_{N2}/V_{N4}/V_{N6}}$, i.e., (221)/(122)/(212)

$$P_{\rm HE} = \frac{3}{2\gamma}{\rm Re}\left(\bar{\boldsymbol{i}}\frac{\boldsymbol{V_{Ly}}t_y}{T_s}\right), y = 2, 4, 6. \tag{7}$$

As shown in Fig. 8(b), the minimum value of PV port power $P_{H\min}$ can be achieved when all positive small vectors are used. In the case of rate ac power, $P^*_{\rm ac} = P_H + P_L$ should be satisfied. Where $P^*_{\rm ac}$ is the rated ac power. Hence, $P_{H\min}$ can be calculated as

$$\begin{aligned} P_{H\min} &= P^*_{\rm ac} - \frac{3}{2}{\rm Re}(\bar{\boldsymbol{i}}(\boldsymbol{V_{Py}} + \boldsymbol{V_{Py+1}})) \\ &= P^*_{\rm ac} - \frac{3}{2(1-\gamma)}{\rm Re}\left(\bar{\boldsymbol{i}}\frac{(\boldsymbol{V_{Ly}}t_y + \boldsymbol{V_{Ly+1}}t_{y+1})}{T_s}\right), y = 1, 3, 5. \end{aligned} \tag{8}$$

Considering that (211) shows lower power losses than (221) in Sector I, (211) is set to have priority in the power distribution process. In summary, the selected negative small vectors in the power distribution process are shown in Table IV. Due to the odd negative small vector $\boldsymbol{V_{N1}/V_{N3}/V_{N5}}$, i.e., (211)/(121)/(112) only switching once to zero vector (111), they are set to have priority in the process of power distribution.

2) Power Distribution Flowchart: Fig. 9 shows the flowchart of the proposed power distribution strategy. The reference output power of PV port P^*_H can be achieved by the power management strategy. P^*_H should not exceed the power distribution range. When $P^*_H \le P_{\rm HO}$, the reference PV port output power can be only supported by the odd negative small vector $\boldsymbol{V_{N1}/V_{N3}/V_{N5}}$, i.e., (211)/(121)/(112). In this case, only regulating $k_{\rm NO}$ is required. Then, $k_{\rm NO}$ can be expressed as

$$k_{\rm NO} = \frac{2\gamma T_s P^*_H}{3{\rm Re}(\bar{\boldsymbol{i}}\boldsymbol{V_{Ly}}t_y)}, y = 1, 3, 5. \tag{9}$$

Once the reference power $P^*_H > P_{\rm HO}$, the even negative small vector $\boldsymbol{V_{N2}/V_{N4}/V_{N6}}$, i.e., (221)/(122)/(212), has to participate in supplying the PV port output power. The proportional factor can be calculated as

$$k_{\rm NE} = \frac{2\gamma T_s (P^*_H - P_{\rm HO})}{3{\rm Re}(\bar{\boldsymbol{i}}\boldsymbol{V_{Ly}}t_y)}, y = 2, 4, 6 \tag{10}$$

where $k_{\rm NE}$ is the proportional factor for regulating the even large vector $\boldsymbol{V_{Ly}}(y = 2, 4, 6)$, $0 \le k_{\rm NE} \le 1$.

3) Power Distribution Range Analysis: Fig. 10 shows the power distribution range versus different dc-port voltage ratios. The reference power of PV port P^*_H should be within the aforementioned power distribution range. Once P^*_H is out of the power distribution range, the modulation will fall outside the linear zone. It can be seen from Fig. 10 that the dc-port voltage ratios have a significant influence on the power distribution range. When $\gamma < \gamma_0$, the minimum value of PV port power is 0, i.e., the flexibility of power distribution is limited. The power distribution range decreases with the increase of the dc-port voltage ratio. The reason is that a large dc-port

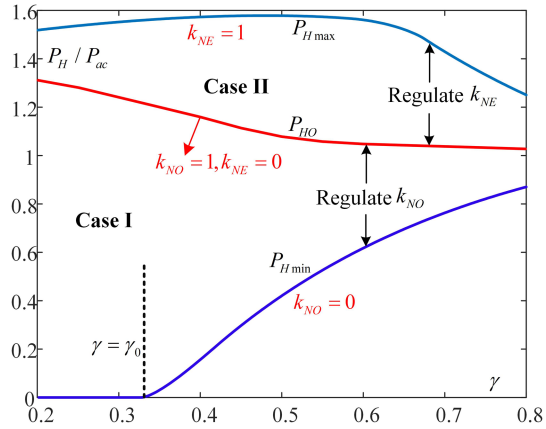

Fig. 10. Power distribution range versus different DC-port voltage ratios.

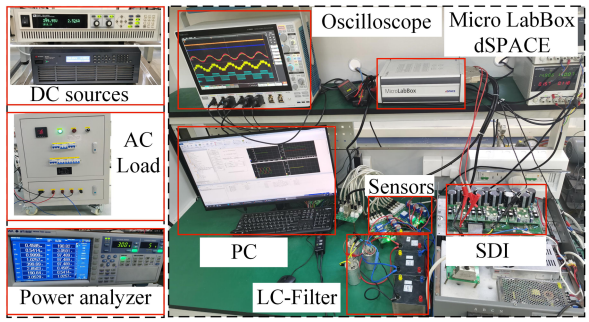

Fig. 11. Experimental test platform.

TABLE V
PARAMETERS OF THE TEST SYSTEM

Battery port voltage	v_l=150-250V
PV port voltage	v_h=400V
DC-side capacitance	$C_1 = C_2$=4920μF
LC- filter inductance	L_1/R_1=3mH/0.4Ω
LC- filter capacitance	C=15μF
Sampling time/frequency	T_s=100μs/f_s=10kHz
Reference grid voltage	V_g^*=110V
Reference grid frequency	f_g^*=50Hz
Reference grid active power	P_{ac}^*=1000W
Reference grid reactive power	Q_{ac}^*=0var

voltage ratio would decrease the freedom of degree provided by the small vectors. It is suggested to set the dc-port voltage ratios as 0.35–0.65 to obtain a wider power distribution range.

The switching sequence is also determined by the power distribution range. In case I, $k_{\rm NE}=0$ should be satisfied, and regulating $k_{\rm NO}$ is required. As a result, only the odd small vectors (211) would be used in the output voltage vector synthesis. In case II, regulating $k_{\rm NE}$ is required. Hence, even small vectors (221) would be used in the output voltage vector synthesis.

D. Duty Cycle Calculation for Upper and Lower Legs

As shown in Fig. 9, duty cycle calculation should be conducted after parameter design. For the sake of simplicity, only the duty cycles in Sector I are discussed. The duty cycles for negative small vectors can be calculated as follows:

$$\begin{cases} d_{\rm NO} = \frac{k_{\rm NO} t_1}{T_s} \\ d_{\rm NE} = \frac{k_{\rm NE} t_2}{T_s} \end{cases} \tag{11}$$

where $d_{\rm NO}/d_{\rm NE}$ indicates the duty cycle for the odd/even negative small vector.

In Sector I, the switching states in phase a are 2 and 1. Then, the duty cycles in phase a can be expressed as follows:

$$\begin{cases} d_{\rm La} = 1 \\ d_{\rm Ha} = \frac{d_{\rm NO}+d_{\rm NE}}{\gamma} \end{cases} \tag{12}$$

where $d_{\rm Ha}/d_{\rm La}$ is the duty cycle for S_{a1}/S_{a2}. Then, the duty cycles in phase b can be expressed as follows:

$$\begin{cases} d_{Lb} = 1 - \frac{t_1/T_s - d_{\rm NO}}{1-\gamma} \\ d_{Hb} = \frac{d_{\rm NE}}{\gamma} \end{cases} \tag{13}$$

where d_{Hb}/d_{Lb} is the duty cycle for S_{b1}/S_{b2}. In Sector I, the switching states in phase c are 1 and 0. Then, the duty cycles in phase c can be expressed as follows:

$$\begin{cases} d_{Lc} = 1 - \frac{(t_1+t_2)/T_s - d_{\rm NO} - d_{\rm NE}}{1-\gamma} \\ d_{Hc} = 0 \end{cases} \tag{14}$$

where d_{Hc}/d_{Lc} is the duty cycle for S_{c1}/S_{c2}.

It can be concluded that the proposed strategy is easy to implement due to the complicated calculations caused by the uneven space vector diagram being avoided. Moreover, flexible power allocation of between the PV unit and battery can be achieved by decomposing the reference voltage vector.

IV. Experimental Results and Discussion

A. Experimental Test Platform Description

To verify the effectiveness of the proposed strategy, a downscale experimental test platform is established in the laboratory. Fig. 11 gives the experimental test platform. The PV-battery hybrid systems are simulated by two bidirectional programmable dc sources (IT6526 C and KEYSIGHT RP7961 A). In this study, the voltage of the PV port is set as 400 V, and the voltage of the battery port is set as 150–250 V. The SDI is implemented by three insulated-gate bipolar transistor power modules (Infineon F3L75R07W2E3). The ac grid is operated in islanded microgrid mode, and the ac load is connected to the SDI via the LC filter. The power analyzer WT1803E is used to calculate system efficiency. The controller Micro LabBox dSPACE DS1202 is used to conduct the proposed strategy, and a Xilinx is adopted to output the gate signals for switches. The control frequency and switching frequency are both set as 10 kHz. All the experimental results are captured by an eight-channel oscilloscope. Parameters of the test platform are shown in Table V. The reference ac active/reactive power is set as $P_{\rm ac}^* = 1000{\rm W}/Q_{\rm ac}^* = 0{\rm var}$.

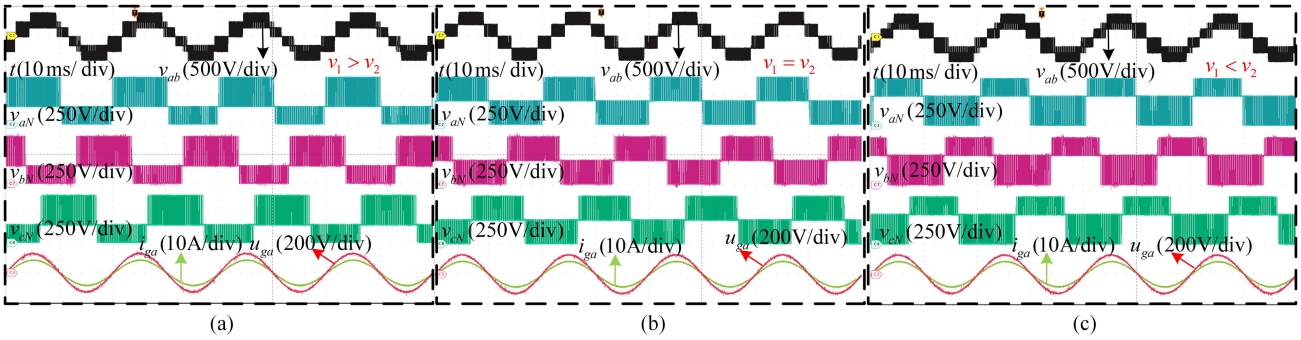

Fig. 12. Steady-state results under variable DC-port voltages. (a) $v_1 > v_2$. (b) $v_1 = v_2$. (c) $v_1 < v_2$. From top to bottom, waveform is line-to-line voltage v_{ab}, phase voltage $v_{aN}/v_{bN}/v_{cN}$, and grid voltage/current u_{ga}/i_{ga}.

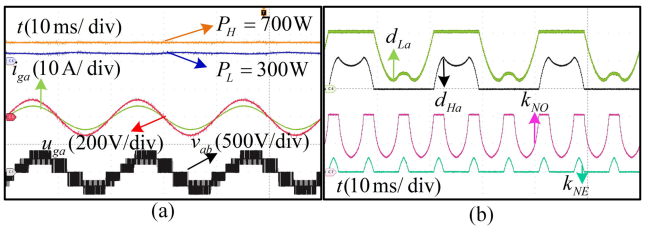

Fig. 13. Power distribution results under $P_H < P_{\text{ac}}$. (a) DC-port output power P_H/P_L, grid voltage/current u_{ga}/i_{ga}, and line-to-line voltage v_{ab}. (b) Duty cycle $d_{\text{La}}/d_{\text{Ha}}$ and parameter $k_{\text{NO}}/k_{\text{NE}}$.

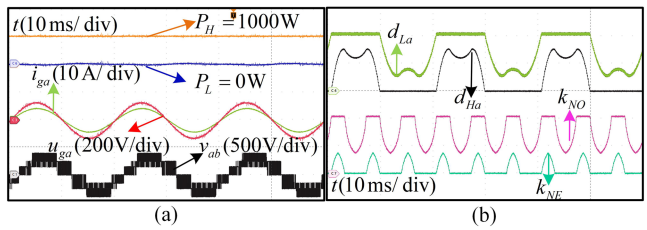

Fig. 14. Power distribution results under $P_H = P_{\text{ac}}$. (a) DC-port output power P_H/P_L, grid voltage/current u_{ga}/i_{ga}, and line-to-line voltage v_{ab}. (b) Duty cycle $d_{\text{La}}/d_{\text{Ha}}$ and parameter $k_{\text{NO}}/k_{\text{NE}}$.

B. Steady-State Performance

To verify the effectiveness of the proposed strategy, the steady-state tests under variable dc-port voltages and different power distribution are carried out.

1) Steady-State Performance Under Variable DC-Port Voltages: Fig. 12 shows steady-state results under variable dc-port voltages: (a) $v_1 > v_2$, (b) $v_1 = v_2$, (c) $v_1 < v_2$. From top to bottom, waveform is line-to-line voltage v_{ab}, phase voltage $v_{aN}/v_{bN}/v_{cN}$, and grid voltage/current u_{ga}/i_{ga}. The voltages of battery port are set as 150 V, 200 V, and 250 V in Fig. 12(a)–(c). The unbalanced line-to-line and phase voltages are caused by the variable dc-port voltages. The steady-state tests in Fig. 12 are conducted in the case of rated active/reactive power, i.e., $P^*_{\text{ac}} = 1000\text{W}/Q^*_{\text{ac}} = 0\text{var}$. Although the dc-port voltages are unbalanced, desirable grid voltage and current can be achieved. Therefore, the proposed strategy is effective for unbalanced dc-port voltage conditions.

2) Results of Power Allocation Under $v_1 < v_2$: Figs. 13– 15 show the different power distribution results under $P_H < P_{\text{ac}}$, $P_H = P_{\text{ac}}$, and $P_H > P_{\text{ac}}$. These tests are conducted under the reference ac grid power conditions, i.e., $P_{\text{ac}} = 1000$ W, $Q_{\text{ac}} = 0$ var. In Fig. 13, the PV unit and battery are used to supply the ac grid together, i.e., $P_H = 700$ W, $P_L = 300$ W. The PV unit is utilized to support the ac grid alone in Fig. 14, i.e., $P_H = 1000$ W, $P_L = 0$ W. In Fig. 15, the PV unit is adopted to supply ac grid and charge the battery simultaneously, i.e., $P_H = 1200$ W, $P_L = -200$ W. The results of duty cycle $d_{\text{La}}/d_{\text{Ha}}$ and parameter $k_{\text{NO}}/k_{\text{NE}}$ are also consistent with the theoretical analysis in Section III. Although the power distribution conditions are variable, beneficial line-to-line/phase voltage and grid voltage/current can be obtained. Hence, the proposed strategy can distribute dc-port power flexibly.

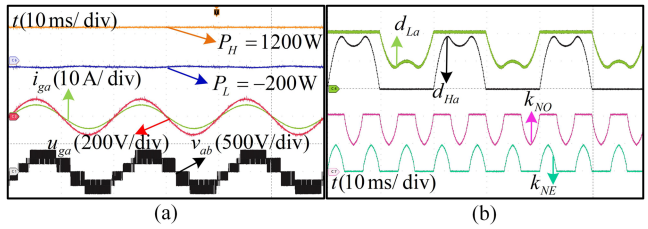

Fig. 15. Power distribution results under $P_H > P_{\text{ac}}$. (a) DC-port output power P_H/P_L, grid voltage/current u_{ga}/i_{ga}, and line-to-line voltage v_{ab}. (b) Duty cycle $d_{\text{La}}/d_{\text{Ha}}$ and parameter $k_{\text{NO}}/k_{\text{NE}}$.

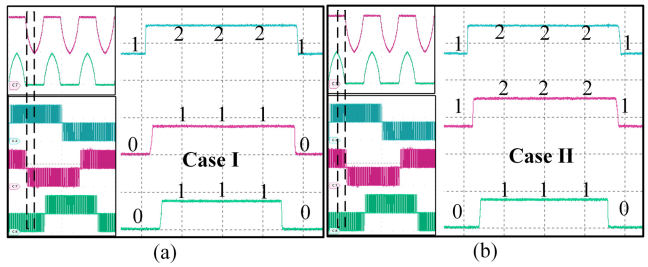

Fig. 16. Switching sequence in Sector I under different power distribution cases. (a) Case I. (b) Case II.

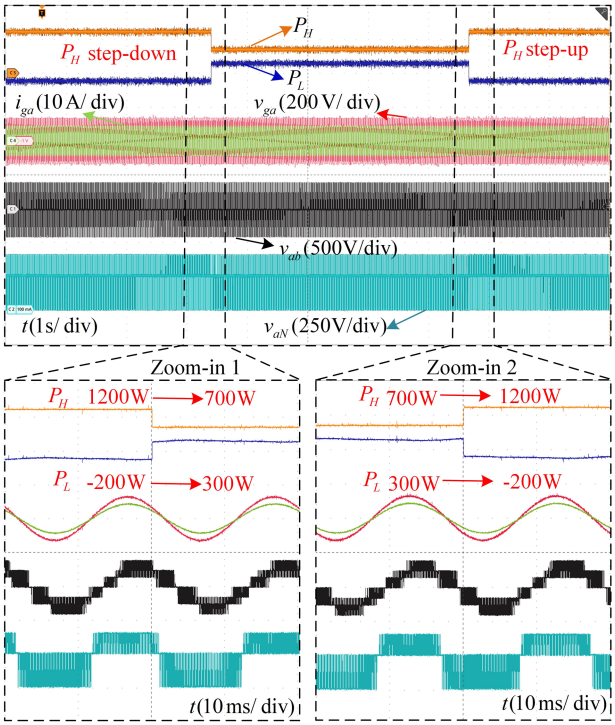

Fig. 17. Dynamic performance of variable DC-port power under constant AC grid power.

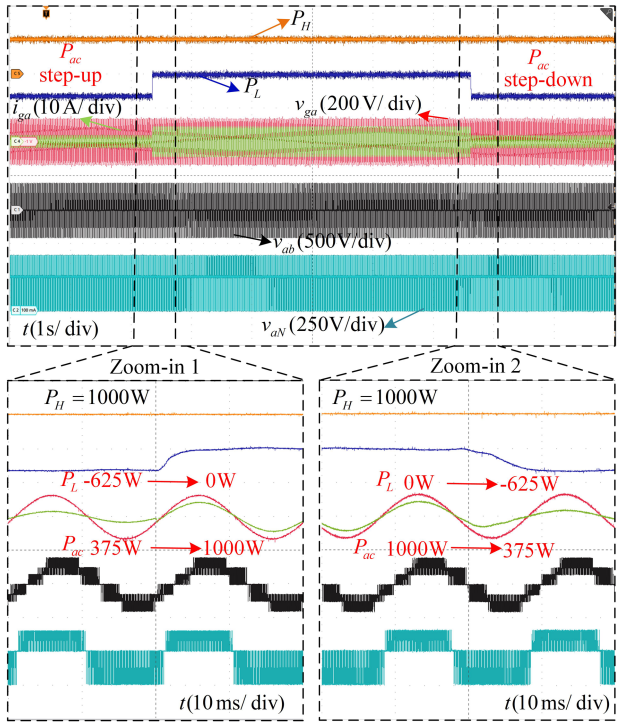

Fig. 18. Dynamic performance of variable AC grid power tests under constant PV generation.

3) Results of Switching Sequence: Fig. 16 shows the switching sequence in Sector I under different power distribution cases: (a) case I, (b) case II. In Fig. 16(a), the switching sequence is 100-200-210-211-210-200-100 in one switching cycle. In Fig. 16(b), the switching sequence is 110-210-220-221-220-210-110 in one switching cycle. Seven-segment PWM signals can be achieved in Sector I. The experimental results of the switching sequence are consistent with the theoretical analysis in Section III. The odd small vector (211) and even small vector (221) are used in case I and case II, respectively.

C. Dynamic Performance

To verify the dynamic performance of the proposed strategy, the variable dc-port power and ac grid power tests are carried out.

1) Dynamic Results of Variable DC-Port Power Under Constant AC Grid Power: Fig. 17 shows the dynamic performance of variable dc-port power under constant ac grid power, which indicates the conditions of variable PV generation. As shown in the zoom-in figure on the left, P_H changes from 1200 to 700 W, and P_L changes from -200 to 300 W. Similar dynamic results can be realized in the zoom-in figure on the right. Although dc-port power has been changed, grid voltage/current u_{ga}/i_{ga} and line-to-line/phased voltage v_{ab}/v_{aN} are stable as desired. It can be concluded that the proposed strategy has fast dynamic performance under variable dc-port power cases.

2). Dynamic Results of Variable AC Grid Power Tests Under Constant PV Generation: Fig. 18 shows the dynamic performance of variable ac grid power tests under constant PV generation. The PV output power is regulated as a constant value, i.e., $P_H = 1000$ W. P_{ac} changes from 375 to 1000 W in the zoom-in figure on the left, and P_{ac} changes from 1000 to 375 W in the zoom-in figure on the right. The battery is used to compensate for the power difference between P_H and P_{ac}. The grid current i_{ga} changes quickly when the ac grid power changes. Although the ac grid power has been changed, grid voltage v_{ga} and phase voltage v_{aN} keep stable. Therefore, the proposed solution offers smooth dynamic performance in the case of variable ac grid power.

D. Comparison With Conventional Power Distribution Strategies

To verify the advantages of the proposed method, comparisons with conventional SVM-based power distribution methods are carried out. Three different conventional methods are conducted. Method 1 is the virtual SVM in [33]. Method 2 is the modified SVM in [34]. Method 3 is the decoupled model-based modulation in [35]. For a fair comparison, the tests are conducted with the same physical parameters, and the grid-side controller is also designed with the same gain constant and bandwidth. In this article, comparisons include underlying principles, computational burden, steady-state/dynamic performance, current quality, and system efficiency.

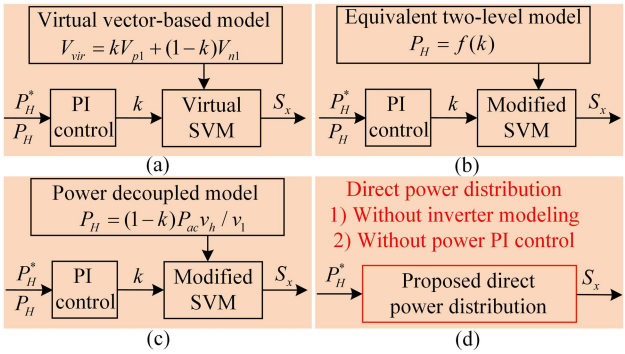

Fig. 19. Power distribution underlying principle comparison. (a) Method 1. (b) Method 2. (c) Method 3. (d) Proposed method.

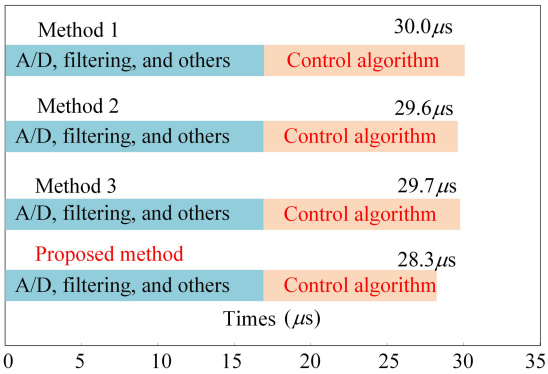

Fig. 20. Execution time of different power distribution methods.

1) Underlying Principle Comparison: Fig. 19 illustrates the power distribution underlying principle comparison: (a) method 1, (b) method 2, (c) method 3, (d) proposed method.

In conventional methods, the modeling for the inverter system under asymmetric vector diagrams is required. Moreover, a PI controller is used to track P_H^* and generate the power distribution factor for the SVM. In summary, the conventional PI control-based methods realize power distribution in an indirect way [33], [34], [35]. As shown in Fig. 19(d), the proposed method can obtain direct power distribution in the modulation layer without inverter modeling and outer loop control. From the perspective of the power distribution underlying principle, the proposed method simplifies the control algorithm effectively.

2) Computational Burden Comparison: Fig. 20 gives the execution time of different power distribution methods. The execution time of different methods is tested by dSPACE ControlDesk. Different power distribution methods spend the same amount of time to carry out A/D conversion, data filtering, communication, protection module, and so on. The conventional methods show longer execution times to realize power control than the proposed method. Method 1 shows the longest execution time due to the uneven voltage vector being directly used in the modulation process. Due to the power distribution control algorithm being simplified, the proposed method shows the shortest execution time.

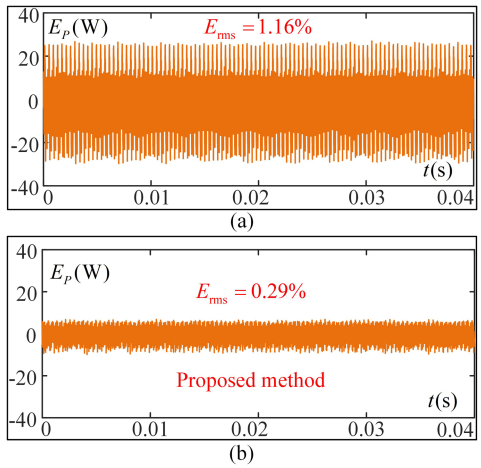

Fig. 21. Steady-state errors of PV port power using different methods. (a) Power tracking error of conventional PI control-based methods. (b) Power tracking error of the proposed method.

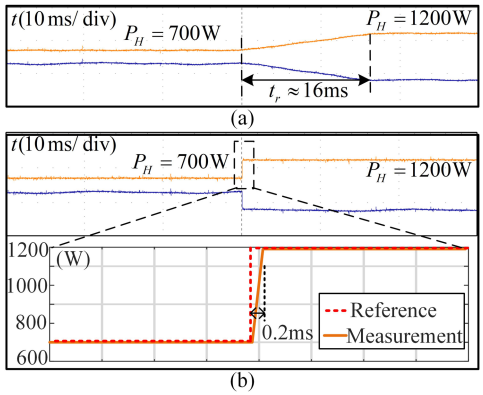

Fig. 22. Dynamic results of different methods under variable DC-port power tests. (a) Dynamic results of conventional PI control-based methods. (b) Dynamic results of the proposed method.

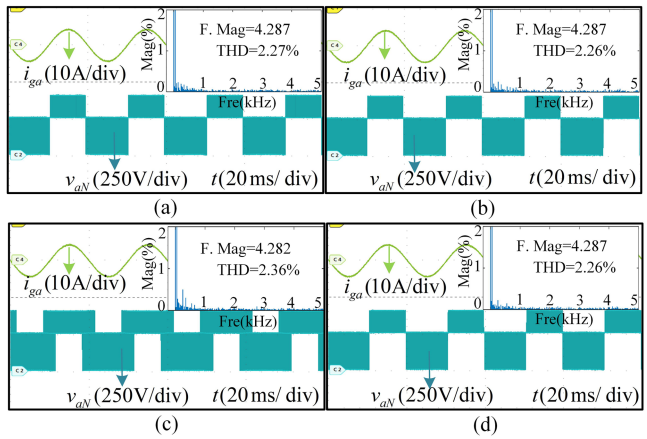

Fig. 23. Current quality comparison between different methods. (a) Method 1. (b) Method 2. (c) Method 3. (d) Proposed method. From top to bottom, the waveform is grid current i_{ga}, graphs of THDs, and phase voltage v_{aN}.

TABLE VI
EXPERIMENTAL RESULTS OF DIFFERENT POWER DISTRIBUTION STRATEGIES FOR SDI

REF	Method	Execution time (μs)	Steady-state E_{rms} (%)	Dynamic t_r (ms)	Current THD (%)	Average efficiency (%)
[33]	Method 1	30.0	1.16	16	2.27	97.61
[34]	Method 2	29.6	1.16	16	2.26	97.62
[35]	Method 3	29.7	1.16	16	2.36	97.21
-	Proposed	28.3	0.29	0.2	2.26	97.62

3) Steady-State/Dynamic Performance Comparison: In this comparison, methods 1, 2, and 3 are conducted with the same PI controller parameters. Fig. 21 gives the steady-state errors of PV port power using different methods: (a) power tracking error of conventional PI control-based methods, (b) power tracking error of the proposed method. The steady-state comparison tests are conducted in the case of $P_H^* = 1000$ W. In Fig. 21, the power tracking error E_p is defined as $E_p = P_H - P_H^*$. The relative root mean square (RMS) error E_{rms} is used to describe the control accuracy, which can be calculated as:

$$E_{\text{rms}} = \frac{||E_p||_2}{||P_H^*||_2} * 100\%. \tag{15}$$

As shown in Fig. 21, the E_{rms} of the conventional PI control-based methods and the proposed method are 1.16% and 0.29%, respectively. Fig. 22 gives the dynamic results of different methods under variable dc-port power tests: (a) dynamic results of conventional PI control-based methods, (b) dynamic results of the proposed method. The transient times t_r of conventional methods are around 16 ms. The transient time t_r of the proposed method is 0.2 ms.

Figs. 21 and 22 indicate that the proposed method shows better steady-state and dynamic performance than conventional methods. The reason is that power distribution can be directly realized in the modulation layer without the additional power control loop.

4) Current Quality Comparison: Fig. 23 shows the current quality comparison between different methods: (a) method 1, (b) method 2, (c) method 3, (d) proposed method.

These tests are conducted with $v_1 < v_2$ in the case of $P_H = P_{\text{ac}}$. It can be concluded from the phase voltage that method 1, method 2, and the proposed method output seven-segment PWM signals. Method 3 generates nine-segment PWM signals. The graphs of THDs are also added in Fig. 23. The THDs of conventional methods are 2.27%, 2.26%, and 2.36%. And the THD of the proposed method is 2.26%. The higher THD in method 3 is caused by the nine-segment PWM signals. Hence, the grid current quality of the proposed method, method 1, and method 2 is better than that of method 3.

5) System Efficiency Comparison: Fig. 24 shows the power analyzer-based system efficiency test circuit. W_H and W_L are the output power of the PV-battery hybrid system. W_{AC1} and W_{AC2} are the active power on the ac side. The efficiency results are obtained by the power analyzer YOKOGAWA WT1803E, which can be calculated as

$$\eta_s = \frac{W_{\text{AC1}} + W_{\text{AC2}}}{W_H + W_L}. \tag{16}$$

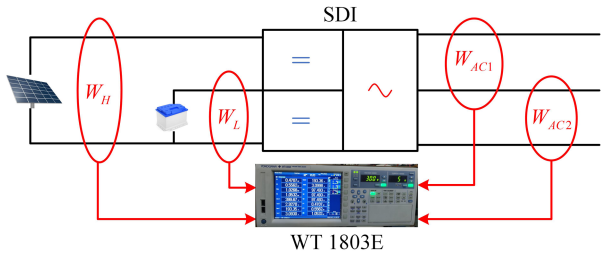

Fig. 24. Power analyzer-based system efficiency test circuit.

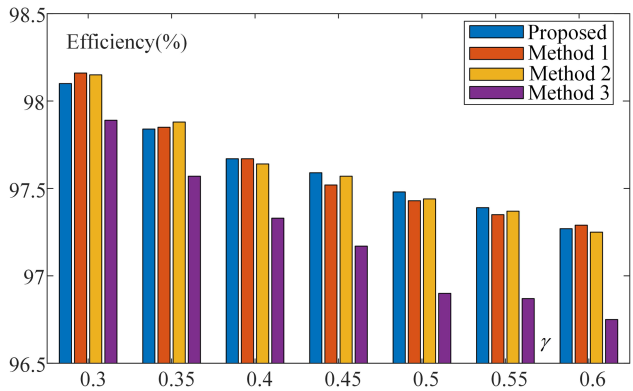

Fig. 25. System efficiency of different power distribution methods under variable DC-port voltage ratio γ.

Fig. 25 shows the system efficiency of different power distribution methods under variable dc-port voltage ratio γ. As shown in Fig. 25, the efficiency of method 3 is around 0.4% lower than that of methods 1, 2, and the proposed method. The lower system efficiency of method 3 is caused by the high-loss phase voltage in Fig. 23. The efficiency of the proposed strategy is as high as that of methods 1 and 2.

The experimental results of different power distribution strategies for SDI are summarized in Table VI, including the execution time, steady-state E_{rms}, transient time t_r, grid current THD, and average efficiency. Not only is the steady-state/dynamic performance effectively improved by the proposed method, but desirable grid current quality and system efficiency can also be obtained.

V. CONCLUSION

In this article, a direct power distribution strategy is proposed for SDI, which achieves flexible power control via the modulation technique by decomposing the reference voltage into large and small vectors. The analytical relationship between

dc-port power and split vector offers a detailed parameter guideline for power distribution control. Compared to conventional SVM-based power distribution strategies, the proposed direct power distribution strategy has effectively reduced the algorithm execution time and improved the steady-state/dynamic response. In addition, high-quality grid current and high system efficiency can be achieved. The proposed method focuses on the dc-port active power allocation and can also handle nonunity power factor conditions.

However, the leakage current caused by the common mode voltage is not mentioned in this article, which causes electromagnetic interference and even system safety problems. In the future, the common-mode voltage suppression will be conducted.

REFERENCES

[1] K. Rahbar, C. C. Chai, and R. Zhang, "Energy cooperation optimization in microgrids with renewable energy integration," *IEEE Trans. Smart Grid*, vol. 9, no. 2, pp. 1482–1493, Mar. 2018.

[2] F. Nejabatkhah and Y. W. Li, "Overview of power management strategies of hybrid AC/DC microgrid," *IEEE Trans. Power Electron.*, vol. 30, no. 12, pp. 7072–7089, Dec. 2015.

[3] Y. Yang, Q. Ye, L. J. Tung, M. Greenleaf, and H. Li, "Integrated size and energy management design of battery storage to enhance grid integration of large-scale PV power plants," *IEEE Trans. Ind. Electron.*, vol. 65, no. 1, pp. 394–402, Jan. 2018.

[4] Y. Pan, A. Sangwongwanich, Y. Yang, and F. Blaabjerg, "Distributed control of islanded series PV-battery-hybrid systems with low communication burden," *IEEE Trans. Power Electron.*, vol. 36, no. 9, pp. 10199–10213, Sep. 2021.

[5] Q. Zhang and K. Sun, "A flexible power control for PV-battery hybrid system using cascaded H-bridge converters," *IEEE J. Emerg. Sel. Topics Power Electron.*, vol. 7, no. 4, pp. 2184–2195, Dec. 2019.

[6] J. Wang, K. Sun, C. Xue, T. Liu, and Y. Li, "Multi-port DC-AC converter with differential power processing DC-DC converter and flexible power control for battery ESS integrated PV systems," *IEEE Trans. Ind. Electron.*, vol. 69, no. 5, pp. 4879–4889, May 2022.

[7] Z. Huang, D. Zhou, L. Wang, Z. Shen, and Y. Li, "A review of single-stage multiport inverters for multisource applications," *IEEE Trans. Power Electron.*, vol. 38, no. 5, pp. 6566–6584, May 2023.

[8] Z. Huang, D. Zhou, Z. Shen, and J. Zou, "Directed graph-based topology derivation method for single-stage multiport inverters," *IEEE Tran. Power Electron.*, vol. 38, no. 11, pp. 14614–14627, Nov. 2023.

[9] K. Luo, D. Zhou, Z. Zhang, J. Zou, and X. Zhou, "Three-dimensional vector multimapping-based power split for single-stage multiport inverter-fed motor drives," *IEEE Trans. Ind. Electron.*, vol. 72, no. 3, pp. 2444–2454, Mar. 2025.

[10] D. Zhou, Y. Mao, and J. Zou, "Double zero-sequence voltage injection-based power distribution control of single-stage multiport inverter-fed hybrid electric vehicles," *IEEE Trans. Ind. Electron.*, vol. 72, no. 2, pp. 1347–1356, Feb. 2025.

[11] M. Schweizer and J. W. Kolar, "Design and implementation of a highly efficient three-level T-type converter for low-voltage applications," *IEEE Trans. Power Electron.*, vol. 28, no. 2, pp. 899–907, Feb. 2013.

[12] J. A. Anderson, D. Marciano, J. Huber, G. Deboy, G. Busatto, and J. W. Kolar, "All-SiC 99.4%-efficient three-phase T-type inverter with DC-side common-mode filter," *Electron. Lett.*, vol. 59, no. 12, 2023, Art. no. e12821.

[13] L. Dorn-Gomba, P. Magne, B. Danen, and A. Emadi, "On the concept of the multi-source inverter for hybrid electric vehicle powertrains," *IEEE Trans. Power Electron.*, vol. 33, no. 9, pp. 7376–7386, Sep. 2018.

[14] D. Zhou, Z. Zhang, Z. Shen, and J. Zou, "Modulated model predictive control of multisource inverters with flexible power distribution," *IEEE Trans. Ind. Electron.*, vol. 71, no. 11, pp. 13732–13741, Nov. 2024.

[15] D. Zhou, K. Luo, Z. Shen, and J. Zou, "Vector-space-decomposition-based power flow control of single-stage-multiport-inverter-fed PMSM drive for hybrid electric vehicles," *IEEE Trans. Ind. Electron.*, vol. 71, no. 8, pp. 8514–8524, Aug. 2024.

[16] E. Fedele, A. Cervone, I. Spina, D. Iannuzzi, and A. D. Pizzo, "Multiobjective vector modulation for improved control of NPC-based multi-source inverters in hybrid traction systems," *IEEE J. Emerg. Sel. Topics Power Electron.*, vol. 10, no. 6, pp. 7464–7474, Dec. 2022.

[17] C. Yan, D. Xu, and W. Chen, "General control scheme for a dual-input three-level inverter," *IEEE Trans. Power Electron.*, vol. 34, no. 2, pp. 1838–1850, Feb. 2019.

[18] Y. Park, S.-K. Sul, C.-H. Lim, W.-C. Kim, and S.-H. Lee, "Asymmetric control of DC-link voltages for separate MPPTs in three-level inverters," *IEEE Trans. Power Electron.*, vol. 28, no. 6, pp. 2760–2769, Jun. 2013.

[19] M. M. Hashempour, M.-Y. Yang, and T.-L. Lee, "An adaptive control of DPWM for clamped-three-level photovoltaic inverters with unbalanced neutral-point voltage," *IEEE Trans. Ind. Appl.*, vol. 54, no. 6, pp. 6133–6148, Nov./Dec. 2018.

[20] Y. Deng, Y. Wang, K. H. Teo, and R. G. Harley, "A simplified space vector modulation scheme for multilevel converters," *IEEE Trans. Power Electron.*, vol. 31, no. 3, pp. 1873–1886, Mar. 2016.

[21] G. Grandi, J. Loncarski, and O. Dordevic, "Analysis and comparison of peak-to-peak current ripple in two-level and multilevel PWM inverters," *IEEE Trans. Ind. Electron.*, vol. 62, no. 5, pp. 2721–2730, May 2015.

[22] S. Das, G. Narayanan, and M. Pandey, "Space-vector-based hybrid pulsewidth modulation techniques for a three-level inverter," *IEEE Tran. Power Electron.*, vol. 29, no. 9, pp. 4580–4591, Sep. 2014.

[23] A. Dekka, B. Wu, N. R. Zargari, and R. L. Fuentes, "A space-vector PWM-based voltage-balancing approach with reduced current sensors for modular multilevel converter," *IEEE Trans. Ind. Electron.*, vol. 63, no. 5, pp. 2734–2745, May 2016.

[24] A. Gupta and A. Khambadkone, "A space vector PWM scheme for multilevel inverters based on two-level space vector PWM," *IEEE Trans. Ind. Electron.*, vol. 53, no. 5, pp. 1631–1639, Oct. 2006.

[25] H. Alawieh, K. A. Tehrani, Y. Azzouz, and B. Dakyo, "A new active common-mode voltage elimination method for three-level neutral-point clamped inverters," in *Proc. 40th Annu. Conf. IEEE Ind. Electron. Soc.*, Oct. 2014, pp. 1060–1066.

[26] X. Wu, G. Tan, Z. Ye, G. Yao, Z. Liu, and G. Liu, "Virtual-space-vector PWM for a three-level neutral-point-clamped inverter with unbalanced DC-links," *IEEE Trans. Power Electron.*, vol. 33, no. 3, pp. 2630–2642, Mar. 2018.

[27] X. Xing, X. Li, F. Gao, C. Qin, and C. Zhang, "Improved space vector modulation technique for neutral-point voltage oscillation and common-mode voltage reduction in three-level inverter," *IEEE Trans. Power Electron.*, vol. 34, no. 9, pp. 8697–8714, Sep. 2019.

[28] Q. Yan, L. Xiao, H. Chen, X. Yuan, H. Xu, and R. Zhao, "An analytical discontinuous space-vector PWM for three-level inverters with unbalanced DC-link voltages," *IEEE Trans. Power Electron.*, vol. 37, no. 7, pp. 7718–7728, Jul. 2022.

[29] H. Wu, J. Wang, T. Liu, T. Yang, and Y. Xing, "Modified SVPWM-controlled three-port three-phase AC–DC converters with reduced power conversion stages for wide voltage range applications," *IEEE Trans. Power Electron.*, vol. 33, no. 8, pp. 6672–6686, Aug. 2018.

[30] Q. Yan et al., "Optimization of the symmetrical SVPWM for three-level T-type inverters with unbalanced and oscillated neutral-point voltages," *IEEE Trans. Ind. Electron.*, vol. 71, no. 4, pp. 4026–4037, Apr. 2024.

[31] S. D. G. Jayasinghe, D. M. Vilathgamuwa, and U. K. Madawala, "Diode-clamped three-level inverter-based battery/supercapacitor direct integration scheme for renewable energy systems," *IEEE Trans. Power Electron.*, vol. 26, no. 12, pp. 3720–3729, Dec. 2011.

[32] H. R. Teymour, D. Sutanto, K. M. Muttaqi, and P. Ciufo, "Solar PV and battery storage integration using a new configuration of a three-level NPC inverter with advanced control strategy," *IEEE Trans. Energy Convers.*, vol. 29, no. 2, pp. 354–365, Jun. 2014.

[33] J. Wang, K. Sun, D. Zhou, and Y. Li, "Virtual SVPWM-based flexible power control for dual-DC-port DC–AC converters in PV–battery hybrid systems," *IEEE Trans. Power Electron.*, vol. 36, no. 10, pp. 11431–11443, Oct. 2021.

[34] L. Liu, D. Zhou, J. Zou, and W. Wang, "Zero-vector-regulation-based closed-loop power distribution strategy for dual-DC-port DC–AC converter-connected PV–battery hybrid systems," *IEEE Trans. Power Electron.*, vol. 38, no. 6, pp. 6956–6968, Jun. 2023.

[35] L. Liu, D. Zhou, J. Zou, and W. Wang, "Decoupled modeling and wide-range power distribution strategy for the multisource inverter in microgrids," *IEEE Trans. Power Electron.*, vol. 38, no. 10, pp. 12078–12090, Oct. 2023.

[36] J. Rocabert, A. Luna, F. Blaabjerg, and P. Rodríguez, "Control of power converters in AC microgrids," *IEEE Trans. Power Electron.*, vol. 27, no. 11, pp. 4734–4749, Nov. 2012.

[37] Z. Yi, W. Dong, and A. H. Etemadi, "A unified control and power management scheme for PV-battery-based hybrid microgrids for both grid-connected and islanded modes," *IEEE Trans. Smart Grid*, vol. 9, no. 6, pp. 5975–5985, Nov. 2018.

[38] P. Sreekumar and V. Khadkikar, "Adaptive power management strategy for effective volt–ampere utilization of a photovoltaic generation unit in standalone microgrids," *IEEE Trans. Ind. Appl.*, vol. 54, no. 2, pp. 1784–1792, Mar./Apr. 2018.

Lijie Liu (Member, IEEE) was born in Chongqing, China. He received the B.S. degree in automation and the Ph.D. degree in control science and engineering from the University of Electronic Science and Technology of China, Chengdu, China, in 2018 and 2024, respectively.

He is currently a Postdoctoral Research Scholar with the School of Electrical Engineering, Chongqing University, Chongqing, China. His current research interests include power electronics and power converters.

Dehong Zhou (Senior Member, IEEE) received the B.Sc. and Ph.D. degrees in control science and engineering from the Huazhong University of Science and Technology, Wuhan, China, in 2012 and 2016, respectively.

From 2016 to 2018, he was a Postdoctoral Research Fellow with Nanyang Technological University, Singapore. From 2018 to 2020, he was a Postdoctoral Fellow with the University of Alberta, Edmonton, AB, Canada. Since 2020, he has been a Full Professor with the School of Automation Engineering, University of Electronic Science and Technology of China (UESTC), Chengdu, China, and Shenzhen Institute for Advanced Study, UESTC, Shenzhen, China. His research interests include power electronics and motor drives.

Jianxiao Zou (Member, IEEE) received the B.S., M.S., and Ph.D. degrees in control science and engineering from the University of Electronic Science and Technology of China (UESTC), Chengdu, China, in 2000, 2003, and 2009, respectively.

He has been a Professor with UESTC, and has been the Vice Dean of Shenzhen Institute for Advanced Study, UESTC since 2020. He was a Visiting Scholar with the University of California, Berkeley, CA, USA, in 2010, and a Senior Visiting Professor with Rutgers, the State University of New Jersey, New Brunswick, NJ, USA, in 2014. His current research interests include control theory and control engineering, renewable energy control technologies, intelligent information processing and control.

Zewei Shen (Member, IEEE) was born in Hubei, China. He received the B.S. degree in control science and engineering and the Ph.D. degree in electrical engineering from the Huazhong University of Science and Technology, Wuhan, China in 2012 and 2020, respectively.

From 2020 to 2022, he was a Postdoctoral Research Fellow with the School of Automation Engineering, University of Electronic Science and Technology of China (UESTC), Chengdu, China, and Shenzhen Institute for Advanced Study, UESTC. From 2022 to 2024, he has been with the University of Electronic Science and Technology of China, Chengdu, China, as a Lecturer. Since 2024, he has been with the University of Electronic Science and Technology of China, Chengdu, China, as an Associate Professor. His current research interests include renewable energy, electromagnetic interference, high power density power supply, and electric motor drives.